Modeling large-scale bioreactors with diffusion equations. Part II: Characterizing substrate, oxygen, temperature, pH, and CO_2 profiles

Pauli Losoi[1], Jukka Konttinen[1], and Ville Santala[1]

[1]Tampereen yliopisto - Hervannan kampus

July 21, 2023

Abstract

Large-scale fermentation processes involve complex dynamic interactions between mixing, reaction, mass transfer, and the suspended biomass. Empirical correlations or case-specific computational simulations are usually used to predict and estimate the performance of large-scale bioreactors based on data acquired at bench scale. In this two-part-study, one-dimensional axial diffusion equations were studied as a general and predictive model of large-scale bioreactors. This second part focused on typical fed-batch operations where substrate gradients are known to occur, and characterized the profiles of substrate, pH, oxygen, carbon dioxide, and temperature. The physically grounded steady-state axial diffusion equations with first- and zeroth-order kinetics yielded analytical solutions to the relevant variables. The results were compared with large-scale *Escherichia coli* and *Saccharomyces cerevisiae* experiments and simulations from the literature, and good agreement was found in substrate profiles. The analytical profiles obtained for dissolved oxygen, temperature, pH, and CO 2 were also consistent with the available data. Distribution functions for the substrate were defined, and efficiency factors for biomass growth and oxygen uptake rate were derived. In conclusion, this study demonstrated that axial diffusion equations can be used to model the effects of mixing and reaction on the relevant variables of typical large-scale fed-batch fermentations.

Modeling large-scale bioreactors with diffusion equations. Part II: Characterizing substrate, oxygen, temperature, pH, and CO_2 profiles

Pauli Losoi * Jukka Konttinen Ville Santala

Faculty of Engineering and Natural Sciences, Tampere University, Hervanta campus, Korkeakoulunkatu 8, Tampere, 33720, Finland

* Corresponding author, pauli.losoi@tuni.fi

Abstract

Large-scale fermentation processes involve complex dynamic interactions between mixing, reaction, mass transfer, and the suspended biomass. Empirical correlations or case-specific computational simulations are usually used to predict and estimate the performance of large-scale bioreactors based on data acquired at bench scale. In this two-part-study, one-dimensional axial diffusion equations were studied as a general and predictive model of large-scale bioreactors. This second part focused on typical fed-batch operations where substrate gradients are known to occur, and characterized the profiles of substrate, pH, oxygen, carbon dioxide, and temperature. The physically grounded steady-state axial diffusion equations with first- and zeroth-order kinetics yielded analytical solutions to the relevant variables. The results were compared with large-scale *Escherichia coli* and *Saccharomyces cerevisiae* experiments and simulations from the literature, and good agreement was found in substrate profiles. The analytical profiles obtained for dissolved oxygen, temperature, pH, and CO_2 were also consistent with the available data. Distribution functions for the substrate were defined, and efficiency factors for biomass growth and oxygen uptake rate were derived. In conclusion, this study demonstrated that axial diffusion equations can be used to model the effects of mixing and reaction on the relevant variables of typical large-scale fed-batch fermentations.

Keywords

bioreactor, scale-up, modeling, reaction, reactor control, diffusion equation

1 Introduction

Substrate-limited large-scale fed-batch bioprocesses are attributed with competition between reaction, mixing, and transfer phenomena, which eventually leads to heterogeneous and suboptimal conditions for the production micro-organism (Enfors et al., 2001). Even though most modeling works have focused on substrate, micro-organisms are known to be affected by dissolved oxygen, pH, temperature, and CO_2 as well (Baez et al., 2009; Caspeta et al., 2009; Risager Wright et al., 2016; Schweder et al., 1999). Thus far the modeling of large-scale bioreactors has been performed with compartment model or computational fluid dynamics (CFD) simulations and scale-down experiments (Haringa et al., 2018; Nadal-Rey et al., 2021; Neubauer & Junne, 2010). Recently, a simple "interaction by exchange with the mean" mixing model utilizing the substrate distribution instead of its axial profile was presented (Maluta et al., 2020), showing that the level of spatial detail in hydrodynamically sophisticated simulations is not strictly necessary to correctly predict biomass yields.

At simplest, the compartment models are one-dimensional or 1D (Bisgaard et al., 2022), and they are essentially discretizations of a diffusion equation. The diffusion equation reproduces tracer curves measured in typical high aspect ratio bioreactors, as it captures the limiting mechanism of mixing, the turbulent axial dispersion (Kawase & Moo-Young, 1989; Machon & Jahoda, 2000; Pinelli & Magelli, 2000). Coupled with suitable approximations to biologically relevant kinetics, the mathematics of diffusion could permit analytical solutions to profiles and distribution functions of the relevant variables in large-scale fed-batch processes. Such results could even be used to derive efficiency factors, which relate with a single number the performance at the large scale to a homogeneous situation (Delvigne et al., 2005).

The aim of this two-part study was to develop a general model of mixing and reaction in typical large-scale stirred fed-batch bioreactors using 1D diffusion equations. The first part derived a predictive formula for the axial diffusivity. This second part focused on predicting and characterizing the profiles of substrate, pH, dissolved oxygen, temperature, and gaseous CO_2 using analytically soluble 1D steady-state diffusion equations with zeroth- and first-order kinetics. The cumulative distribution and probability density functions were also defined for the substrate. The modeling was compared against both experimental (Bylund et al., 1998; Larsson et al., 1996; Xu, Jahic, Blomsten, & Enfors, 1999) and numerical (Larsson et al., 1996; Losoi et al., 2022; Pigou & Morchain, 2015) literature data concerning *Escherichia coli* and *Saccharomyces cerevisiae* fed-batch fermentations. The model solutions were also utilized to derive simple efficiency factor formulae for oxygen uptake and biomass growth rates.

2 Materials and methods

2.1 Experiments and simulations from literature

The large-scale experiments by Bylund et al. (1998), Larsson et al. (1996), and Xu, Jahic, Blomsten, and Enfors (1999) were used as a reference for the modeling. The cited works reported glucose concentrations measured at

top, middle, and bottom sections of the reactors and biomass concentrations. Dissolved oxygen tensions were also monitored with one probe at the middle (Larsson et al., 1996) or two probes at the middle and the bottom (Xu, Jahic, Blomsten, & Enfors, 1999). Bylund et al. (1998) did not report the probe location, so it was assumed here to be at the middle as well. The control values for pH and temperature were provided in the referenced works. The liquid volumes were from 8 m^3 up to 22 m^3. Table 1 lists relevant variables and quantities regarding the experiments. The axial diffusivities and mixing times were calculated from operating conditions as in Part I of this study (Losoi et al., 2023). Bylund et al. (1998) reported ranges of stirrer and gas flow rates, and here the midpoint of these ranges was used as the operating condition. The mean substrate concentrations shown in Table 1 refer to time points with constant feeds and 20 $g\,L^{-1}$ biomass concentrations. Altogether the substrate data from these references included 96 time points with three values each measured at the top, middle, and bottom of the reactors. Gas holdups were determined from the references from the reported liquid volumes and total dispersion heights, but for Bylund et al. (1998) experiments the holdups were estimated here using a correlation fitted for large scale (Vrábel et al., 2000). Larsson et al. (1996) and Xu, Jahic, Blomsten, and Enfors (1999) reported $k_L a = 180\,h^{-1}$ for their setups, and by using the functionalities of the $k_L a$ correlations reviewed by Gabelle et al. (2011), it was estimated that $k_L a$ should have been approximately 70 %–80 % of that value in the Bylund et al. (1998) experiments. For simplicity, the same $k_L a = 180\,h^{-1}$ was used also for the Bylund et al. (1998) experiments. Some of the operating conditions for the Xu, Jahic, Blomsten, and Enfors (1999) experiment were determined using literature based on the same large-scale reactor (Vrábel et al., 1999; Vrábel et al., 2001). The *E. coli* kinetic parameters determined by Xu, Jahic, and Enfors (1999) were used both for Bylund et al. (1998) and Xu, Jahic, Blomsten, and Enfors (1999) experiments.

The large-scale simulations in 20 m^3 liquid volumes by Larsson et al. (1996), Losoi et al. (2022), and Pigou and Morchain (2015) were used as a further reference. Larsson et al. (1996) reported glucose contours obtained with CFD simulations with standard Monod kinetics (Figure 7 in Larsson et al., 1996). The cumulative distribution function (CDF) of their simulated substrate concentrations was estimated here by approximating the areas between concentration contour lines. Pigou and Morchain (2015) used a two-dimensional (2D) compartment model and a metabolic model and provided heat maps and values of glucose concentration and also biomass concentrations (Figures 9 and 7b in Pigou and Morchain, 2015). Their results were considered here as CDFs and also as radially averaged 1D axial profiles. Our previously published results (Table 1 in Losoi et al., 2022) were obtained with a three-dimensional (3D) compartment model and standard Monod kinetics. The diffusivity for Larsson et al. (1996) simulations was kept the same as for their experiments (Table 1). For Pigou and Morchain (2015) simulations a diffusivity of $d = 0.0659\,m^2\,s^{-1}$ was calculated using the transfer resistance analogy concept presented in Part I of this study (Losoi et al., 2023) and the provided exchange, circulation, and induced flow rates (Appendix B in Pigou and Morchain, 2015). A $d = 0.106\,m^2\,s^{-1}$ diffusivity was estimated for Losoi et al. (2022) simulations from the reported 95 % standard deviation based mixing time of 154 s using the corresponding formula from Part I of this study (Equation 7 in Losoi et al., 2023).

2.2 Linearization of substrate consumption rates

For the model used here, volumetric (liquid-phase) substrate consumption rates r_S ($\mathrm{g\,L^{-1}\,h^{-1}}$) were linearized into $r_S = k_S S$, where k_S is first-order rate-pseudoconstant ($\mathrm{h^{-1}}$), a function of substrate concentration, and S the substrate concentration ($\mathrm{g\,L^{-1}}$). Using this definition, the rate-pseudoconstants were evaluated using mean consumption rates and mean concentrations. Experimental mean concentrations were estimated here as weighted averages of the three measured concentrations such that the individual sampling locations were given weights according to the working height that they represented, although the weighing had only little effect on the mean. Simulated mean concentrations were either provided directly in the references or they could be calculated from the data. When comparing the model with experiments, the volumetric substrate consumption rate r_S was assumed to equal the volumetric feed rate Q_S (steady-state assumption), which was obtained from the references. When considering previously published simulations, the kinetics used in the reference were analytically linearized and the first-order rate-pseudoconstant k_S was evaluated with the mean concentration of substrate, $\langle S \rangle$. Larsson et al. (1996) used standard Monod-kinetics for substrate consumption, which yielded

$$k_S = \frac{q_S X}{\langle S \rangle + K_S} \tag{1}$$

as the volumetric substrate consumption's first-order rate-pseudoconstant, where $q_S = 1.7\,\mathrm{g\,g^{-1}\,h^{-1}}$ is biomass-specific maximal substrate consumption rate, X biomass concentration ($\mathrm{g\,L^{-1}}$), and $K_S = 0.18\,\mathrm{g\,L^{-1}}$ Monod constant. The kinetic parameters were $q_S = 1\,\mathrm{g\,g^{-1}\,h^{-1}}$ and $K_S = 0.025\,\mathrm{g\,L^{-1}}$ for Losoi et al. (2022). The substrate consumption rate in the Pigou and Morchain (2015) metabolic model was based on defining an equilibrium biomass growth rate and using a Pirt-form of biomass yield to calculate the anabolic demand of substrate. Their model included also catabolic demand of substrate, which accounted for oxidative capacity and state of the population. Here, the effects of acetate, oxygen, and population state were neglected, which ultimately simplified the first-order rate-pseudoconstant into the same Equation 1, but with

$$\frac{q_S}{\mathrm{g\,g^{-1}\,h^{-1}}} = 1.28 + \left(1 + \frac{K_S}{\langle S \rangle}\right) 0.0722 \tag{2}$$

and $K_S = 0.05\,\mathrm{g\,L^{-1}}$. The parameters and biomass concentrations necessary for calculating the rate-constants were directly available in each study.

2.3 Green's function method

The Green's function method (Cole et al., 2010) was used to solve the steady-state 1D diffusion equations with zeroth- and first-order kinetics, or Laplace and Helmholtz equations, respectively. The method centers around integrating the considered equation's impulse response to a volumetric source term under the imposed boundary conditions. Symbolic computation software (`sympy`) was used for some of the derivations.

2.4 Model statistics and uncertainty

Model fits were assessed against the experimentally determined data with the same two coefficients of determination that were used also in Part I of this study (Losoi et al., 2023). R^2 is the conventional coefficient of determination based on residuals $f - y$, whereas Q^2 is an analogous coefficient of determination defined with logarithmic error $q = \log(f/y)$. The error term in both coefficients was also decomposed to systematic and random error components. Details on these metrics are given in Section 2.2 of Part I and Supporting Information: Section S3 of Part I. Like in Part I, the error σ expected in model prediction due to the uncertainty of its N parameters x_i was estimated by propagation of error with zero covariance between parameters: $\sigma_f = \sqrt{\sum_{i=1}^{N} (\partial f/\partial x_i)^2 \sigma_{x_i}^2}$, where σ_i is x_i's standard deviation. In Part I, an error of $\sigma_d/d = 7\,\%$ was determined for the diffusivity parameter d.

2.5 Software

The `Python` programming language version `3.8.5` (www.python.org) was used for all calculations and derivations with the packages `numpy 1.19.2` (Harris et al., 2020), `pandas 1.1.3` (McKinney, 2010; The pandas development team, 2020), `scipy 1.5.2` (Virtanen et al., 2020), and `sympy 1.6.2` (Meurer et al., 2017). Both experimental and simulated previously published data were digitized from original figures with `WebPlotDigitizer` (Rohatgi, 2020) and `GNU Image Manipulation Program 2.10.18` (www.gimp.org).

3 Theoretical aspects

3.1 Substrate profile and distribution

Here, typical fed-batch operations were considered such that both the steady-state approximation $\partial S/\partial t \approx 0$ and negligible dilution $\partial V/\partial t \approx 0$ applied. Assuming spatially constant diffusivity and gas holdup and negligible volume fraction of biomass, the mass balance of substrate with a standard Monod-form uptake rate was

$$d\frac{\partial^2 S}{\partial z^2} + Q_S = \frac{S}{S + K_S} q_S X, \tag{3}$$

where z is the axial coordinate (m) and Q_S the local liquid-phase volumetric source or feed term ($\mathrm{g\,L^{-1}\,h^{-1}}$). However, Equation 3 is not analytically soluble with Monod kinetics, but considering the mean substrate concentration $\langle S \rangle$ as a parameter and approximating the Monod-term $S/(S + K_S)$ in Equation 3 with $S/(\langle S \rangle + K_S)$ as explained in Section 2.2 resulted in a classical Helmholtz equation

$$d\frac{\partial^2 S}{\partial z^2} + Q_S = \frac{q_S X}{\langle S \rangle + K_S} S. \tag{4}$$

A nondimensional form

$$\frac{\partial^2 u}{\partial x^2} + \frac{H^2 Q_S}{d\,\langle S \rangle} = M^2 u \tag{5}$$

was obtained by defining a dimensionless substrate concentration $u = S/\langle S \rangle$ and a dimensionless axial coordinate $x = z/H$. The substrate modulus

$$M = H\sqrt{\frac{q_S X}{d\left(\langle S \rangle + K_S\right)}} \tag{6}$$

is a dimensionless number analogous to the Thiele modulus used in chemical reaction engineering to characterize mass transfer effects in catalytic reactions. In terms of time-scale analysis, the substrate modulus is the square root of the ratio of mixing and substrate consumption time-scales. For example, $M = 2$ indicates that mixing is outperformed by reaction, as the rate of substrate uptake is four times the rate of mixing. A general feel for the modulus and mixing limitations can be given by taking the longest t_{95} (95 % mixing time with probe and feed as wide apart as possible) as the measure of mixing rate according to Equation 5 in Part I of this study (Losoi et al., 2023), $\langle S \rangle = K_S = 0.05\,\mathrm{g\,L^{-1}}$ as the mean substrate concentration and Monod-constant, both quite likely values in fed-batch operations (Bylund et al., 1998, 2000; Castan & Enfors, 2002; Larsson et al., 1996; Xu, Jahic, Blomsten, & Enfors, 1999), and $q_S = 1\,\mathrm{g\,g^{-1}\,h^{-1}}$ as the biomass-specific maximal uptake rate. Under these conditions Equation 6 is simplified to

$$M \approx 0.0862\sqrt{\frac{X}{\mathrm{g\,L^{-1}}}\frac{t_{95}}{\mathrm{s}}}. \tag{7}$$

Another approach to evaluate the modulus is to utilize the steady-state approximation $r_S \approx Q_S$, which gives the modulus as a function of substrate feed rate instead assuming $\langle S \rangle = K_S = 0.05\,\mathrm{g\,L^{-1}}$:

$$M \approx 0.122\sqrt{\frac{Q_S}{\mathrm{g\,L^{-1}\,h^{-1}}}\frac{t_{95}}{\mathrm{s}}}. \tag{8}$$

Tables 2 and 3 list example values for substrate modulus with some common 95 % mixing times, biomass concentrations, and feed rates using Equations 7 and 8, respectively. With over $40\,\mathrm{g\,L^{-1}}$ biomass concentrations or $16\,\mathrm{g\,L^{-1}\,h^{-1}}$ feed rates, mixing limitations ($M > 1$) seem likely even in small-scale reactors with only $t_{95} = 10\,\mathrm{s}$ mixing times. In large-scale reactors, where $t_{95} > 200\,\mathrm{s}$ and longer mixing times are possible, mixing limitations may occur with biomass concentrations as low as $X = 5\,\mathrm{g\,L^{-1}}$ or with feed rates as low as $Q_S = 1\,\mathrm{g\,L^{-1}\,h^{-1}}$.

Equation 5 was solved with the Green's function method (Cole et al., 2010), which allowed flexibility in defining the volumetric source Q_S. Using a Dirac delta point source at x_0, $\delta(x - x_0)$, and insulated boundaries ($\partial u/\partial x = 0$ at both $x = 0$ and $x = 1$), the axial profile of dimensionless substrate concentration was found to be

$$u = \frac{M}{\sinh M}\cosh\left(M\min(x, x_0)\right)\cosh\left(M(1 - \max(x, x_0))\right). \tag{9}$$

Supporting Information: Figure S1 compares the analytical substrate profile with linearized kinetics to profiles determined numerically by finite-volume discretization and with standard Monod kinetics assuming the Monod constant is 0.1, 1, or 10 times the mean substrate concentration. The analytical profile is remarkably close to the numerically solved unsimplified profiles, yielding mostly $R^2 \geq 95$ %. The test case $M = 4$ with $\beta = 0.1$ deviated

substantially from the linearized analytical profile, but this case corresponded to an unlikely situation having both a considerable mixing limitation (time-scale of mixing 16 times the time-scale of reaction) and a high mean concentration of substrate ($\langle S \rangle = 10K_S$). Thus, in the context of the steady-state 1D diffusion equation, linearization is a good approximation to Monod kinetics provided that the mean concentration of substrate is known or can be predicted.

The CDF of (dimensionless) substrate concentration was found by first noting that a randomly chosen point in the reactor obeys the uniform distribution such that the CDF of the (dimensionless) axial coordinate is $F(x) = x$ when $0 \leq x \leq 1$. Solving for x in Equation 9 allowed identifying the substrate's CDF as

$$F(u) = \frac{1}{M}\left(\operatorname{arcosh}\left(\frac{u}{u_{\min}}\right) + \operatorname{arcosh}\left(\frac{\max(u, u_{\text{tres}})}{u_{\text{tres}}}\right)\right). \tag{10}$$

when $u_{\min} \leq u \leq u_{\max}$. Owing to the symmetry of the diffusion equation, feed points at $0 \leq x_0 \leq 0.5$ can be reflected to $0.5 \leq x_0 \leq 1$, and it is easiest to continue by defining $x_0' = \max(x_0, 1 - x_0)$. The minimum concentration is found at the point farthest away from the (reflected) feed, $u_{\min} = u(0, x_0', M)$, the threshold value at the domain boundary closest to feed point, $u_{\text{tres}} = u(1, x_0', M)$, and the maximum at the feed point, $u_{\max} = u(x_0, x_0, M)$. The substrate concentration's probability density function, also known as volume distribution (Morchain et al., 2014), was obtained by differentiating Equation 10 with respect to u:

$$f(u) = \frac{1}{M}\frac{1}{\sqrt{u^2 - u_{\min}^2}} \qquad \text{when } u_{\min} < u < u_{\text{tres}} \tag{11}$$

$$f(u) = \frac{1}{M}\left(\frac{1}{\sqrt{u^2 - u_{\min}^2}} + \frac{1}{\sqrt{u^2 - u_{\text{tres}}^2}}\right) \qquad \text{when } u_{\text{tres}} < u \leq u_{\max}. \tag{12}$$

The density function has discontinuities at $u \in \{u_{\min}, u_{\text{tres}}\}$. The variance σ^2 of substrate concentration is found easiest by integrating spatially $(u(x) - 1)^2$ with respect to x, which yields

$$\sigma^2 = M^2 \frac{x_0 \cosh^2(M(1 - x_0)) + (1 - x_0)\cosh^2(Mx_0)}{2\sinh^2 M} + M\frac{\cosh(M(1 - x_0))\cosh(Mx_0)}{2\sinh M} - 1. \tag{13}$$

3.2 Dissolved oxygen

Based on a time-scale analysis the liquid-phase mixing of dissolved oxygen was surpassed by transfer between gas and liquid phases in the considered references, and by extension in typical fed-batch processes: for example, with Xu, Jahic, Blomsten, and Enfors (1999) configuration the time-scale of mixing was estimated to $(7.9\,\text{m})^2/0.134\,\text{m}^2\,\text{s}^{-1} \approx 466\,\text{s}$, whereas they reported $k_\text{L}a = 180\,\text{h}^{-1}$ corresponding to a 20 s time-scale. The profile of dissolved oxygen was then obtained by a steady-state approximation without mixing assuming that local transfer and consumption rates are equal. The local consumption rate was estimated with spatially dependent zeroth-order kinetics, where the mean oxygen demand rate ODR ($\text{g}\,\text{L}^{-1}\,\text{h}^{-1}$) was determined from the volumetric substrate feed rate using a constant

yield coefficient (Bylund et al., 2000; Xu, Jahic, & Enfors, 1999):

$$\mathrm{ODR} = 0.446\,\mathrm{g\,g^{-1}} Q_S. \tag{14}$$

The local consumption was considered to have the same axial profile as the substrate concentration. The corresponding mass balance was

$$k_\mathrm{L}a(hO_\mathrm{G} - O_\mathrm{L}) = \mathrm{ODR}u, \tag{15}$$

where $k_\mathrm{L}a$ is gas-liquid transfer rate-constant for oxygen (h^{-1}), h Henry's constant for oxygen ($\mathrm{mol_L\,mol_G^{-1}}$, Sander, 2015), O_G gas-phase concentration of oxygen ($\mathrm{g\,L^{-1}}$), O_L liquid-phase concentration of oxygen ($\mathrm{g\,L^{-1}}$), and u local dimensionless concentration of substrate (Equation 9). Solving for liquid-phase oxygen and limiting the values from below to zero yielded

$$O_\mathrm{L}(x) = \max\left(0, hO_\mathrm{G}(x) - \frac{\mathrm{ODR}u(x)}{k_\mathrm{L}a}\right) \tag{16}$$

Local dissolved oxygen tension (DOT) was obtained by dividing O_L by local equilibrium concentration with zero gas-phase conversion, $hO_\mathrm{G}(x)$. In the referenced studies the flow of air into the bioreactors was so high that even with a $1\,\mathrm{g\,g^{-1}}$ consumption of oxygen per substrate the overall gas-phase oxygen conversions could have been 25 %–50 % at most. The effect of gas-phase depletion was then neglected, which simplified the treatment.

The simple zeroth-order formulation allowed approximating the oxygen-limited volume fraction of the reactor directly as the volume fraction where the substrate concentration induced a demand exceeding the transfer rate:

$$1 - F\left(u*, M\right), \tag{17}$$

where the threshold substrate concentration is

$$u* = \frac{\mathrm{OTR}}{\mathrm{ODR}}. \tag{18}$$

Since the maximum demand is found at the feed point x_0, the oxygen transfer rate

$$\mathrm{OTR} = k_\mathrm{L}ahO_\mathrm{G} \tag{19}$$

was evaluated with gas-phase concentration O_G at the feed point's hydrostatic pressure as well.

3.3 Efficiency factors

Using the distribution and density functions derived for substrate, it was possible to derive efficiency factors for oxygen uptake and biomass growth on main substrate. The efficiency factors represent the fraction of oxygen demand satisfied and the fraction of substrate uptake that the population is adapted to continue growing on. The efficiency for oxygen uptake rate was obtained by integrating the substrate-dependent oxygen uptake rate $\mathrm{OUR}(u)$ with respect

to the substrate concentration and dividing this overall volumetric oxygen uptake rate by the overall volumetric oxygen demand rate such that $\mathrm{OUR} = \eta_{\mathrm{OUR}}\mathrm{ODR}$ ($\mathrm{g\,L^{-1}\,h^{-1}}$). At substrate concentrations below the threshold $u*$ (Equation 18), the uptake rate equals the local demand such that $\mathrm{OUR}(u) = \mathrm{ODR}u$, but at concentrations above the threshold the uptake rate is limited to the transfer rate in Equation 19 such that $\mathrm{OUR}(u) = \mathrm{OTR}$. The integral

$$\eta_{\mathrm{OUR}} = \frac{\int_{u_{\min}}^{u_{\max}} f\mathrm{OUR}(u)\mathrm{d}u}{\mathrm{ODR}} = \int_{u_{\min}}^{u*} fu\mathrm{d}u + \frac{\mathrm{OTR}}{\mathrm{ODR}}\int_{u*}^{u_{\max}} f\mathrm{d}u, \tag{20}$$

where f is the substrate's density function, eventually simplified into

$$\eta_{\mathrm{OUR}} = G(u*) + \frac{\mathrm{OTR}}{\mathrm{ODR}}\left(1 - F(u*)\right), \tag{21}$$

where G is the first moment of the substrate distribution:

$$G(u) = \frac{1}{M}\left(\sqrt{u^2 - u_{\min}^2} + \sqrt{\max\left(u, u_{\mathrm{tres}}\right)^2 - u_{\mathrm{tres}}^2}\right). \tag{22}$$

Efficiency of growth on main substrate was determined similarly by utilizing the population balance and adaptation concepts (Morchain & Fonade, 2009; Morchain et al., 2013): the population was assumed to grow at the growth rate $\mu(u)$ allowed by the environment where substrate concentration was below the mean ($u < 1$), and to grow at the mean growth rate $\langle\mu\rangle$ where substrate concentration exceeded the mean. Here the growth rate allowed by the environment was assumed to follow the substrate profile just like the oxygen consumption, $\mu(u) = \langle\mu\rangle\, u$, which yielded

$$\eta_{\mu} = \frac{\int_{u_{\min}}^{u_{\max}} f\mu(u)\mathrm{d}u}{\langle\mu\rangle} = \int_{u_{\min}}^{1} fu\mathrm{d}u + \int_{1}^{u_{\max}} f\mathrm{d}u \tag{23}$$

as the integral. Integration resulted in

$$\eta_{\mu} = G(1) + 1 - F(1). \tag{24}$$

To give an interpretation to the efficiency factors, they can both be transformed into simplistic biomass yield efficiencies. Given an aerobic biomass yield on glucose $Y_0 = 51\,\%$ and an anaerobic yield $Y_1 = 15\,\%$ (Xu, Jahic, & Enfors, 1999), the oxygen-uptake-based yield efficiency was

$$\eta_Y = \eta_{\mathrm{OUR}} + (1 - \eta_{\mathrm{OUR}})\frac{Y_1}{Y_0} \tag{25}$$

The concept is that globally the micro-organism utilizes glucose aerobically as far as possible and that the rest of glucose consumption is anaerobic. For biomass growth a similar yield efficiency can be formulated by using η_{μ}, aerobic yield on glucose $Y_0 = 51\,\%$, and aerobic yield on acetate that has resulted from glucose overflow $Y_1 = 0.667 \times 0.4 = 26.7\,\%$ (Xu, Jahic, & Enfors, 1999). For growth rate efficiency the concept is that the population grows on glucose, but dissimilates glucose to acetate by overflow metabolism when substrate concentration exceeds

the mean and then consumes the acetate later on.

3.4 Temperature

The steady-state temperature profile was determined by using a heat source with the substrate's spatial distribution and a uniform cooling that balanced the heat source across the whole volume. In effect the diffusion equation for temperature had then two zeroth-order kinetic terms, one spatially variable and the other spatially uniform. The balance for temperature was

$$\rho C_p d \frac{\partial^2 T}{\partial z^2} = \Delta H_\mathrm{r} \mathrm{OUR} u - \Delta H_\mathrm{r} \mathrm{OUR}, \tag{26}$$

where $\rho = 1000\,\mathrm{kg\,m^{-3}}$ is the fermentation broth density, $C_p = 4180\,\mathrm{J\,kg^{-1}\,K^{-1}}$ the specific heat capacity of water (Rumble, 2022), T temperature (K), and $\Delta H_\mathrm{r} = 460\,\mathrm{kJ\,mol^{-1}} = 14\,375\,\mathrm{kJ\,kg^{-1}}$ the enthalpy of reaction per oxygen consumed (Doran, 2013). Equation 26 was solved with insulated boundaries and simplified into

$$\theta(x) = \frac{1}{3} + \frac{1}{2M^2}\left(-2u(x) + \cosh(M(1-x_0))(M^2(x^2-1)+2)\right) \qquad \text{when } x \le x_0 \tag{27}$$

$$\theta(x) = \frac{1}{3} + \frac{1}{2M^2}\left(-2u(x) + \cosh(Mx_0)(M^2(x^2-2x)+2)\right) \qquad \text{when } x > x_0 \tag{28}$$

by defining a nondimensional temperature

$$\theta(x) = \frac{T(x) - \langle T \rangle}{M_T} \tag{29}$$

and a temperature coefficient (K)

$$M_T = \frac{\Delta H_\mathrm{r} \mathrm{OUR} H^2}{\rho C_p d}. \tag{30}$$

The substrate modulus M and feed point x_0 define the shape of the temperature profile, but the temperature coefficient M_T defines its magnitude.

3.5 pH control

Addition of base was considered in this work, but addition of an acid would be treated similarly. The pH profiles were estimated by utilizing a steady-state approximation, that can be thought to represent a time point during a pH correction cycle after the initial transient. The source term is the pumping rate localized at the point of addition. A spatially uniform sink term balances the addition rate Q_B ($\mathrm{mol\,L^{-1}\,h^{-1}}$). The resulting balance equation was similar to the temperature but with a Dirac delta point source at x_0:

$$d \frac{\partial^2 C_B}{\partial z^2} = Q_B \left(1 - \delta(x - x_0)\right), \tag{31}$$

which yielded

$$\frac{C_B}{\langle C_B \rangle} = 1 + \frac{Q_B H^2}{\langle C_B \rangle d} \left(\frac{1}{3} + \frac{x^2 + x_0^2}{2} - \max(x, x_0) \right) \tag{32}$$

with insulated boundaries. $\langle C_B \rangle$ is the mean concentration of added base (mol L^{-1}), which is defined by how large a pH change has been imposed on the medium. The local pH was then obtained with the Henderson-Hasselbalch approximation using the medium's buffer concentrations and the local base concentrations. The dimensionless number

$$M = \frac{Q_B H^2}{\langle C_B \rangle d} \tag{33}$$

is the pH modulus, or the ratio of the time-scale of mixing to the time-scale of base addition.

3.6 CO_2 in gaseous phase

The profile of CO_2 was estimated for a tall reactor using plug flow approximation for the gaseous phase. Similarly to the oxygen profile, CO_2 was considered to be released into the gas phase according to the substrate profile after having estimated the overall production rate Q_{CO_2} (g L^{-1} h^{-1}) from the substrate feed rate Q_S using a constant yield coefficient. Here a 1.47 g g^{-1} yield was used, which corresponds to complete oxidation of glucose. The resulting balance equation was

$$\frac{\partial n_{CO_2}}{\partial z} = Q_{CO_2} u, \tag{34}$$

where n_{CO_2} is the molar flow of CO_2 (mol h^{-1}) and Q_{CO_2} the volumetric (gas-liquid dispersion) CO_2 production rate divided by cross-section (mol m^{-1} h^{-1}). Inlet molar flow at the bottom was considered to be zero. The dimensionless profile of CO_2's molar flow in the gas phase integrated to

$$\frac{n_{CO_2}(x)}{Q_{CO_2} H} = \frac{1}{\sinh M} \left(\sinh(M \min(x, x_0)) \cosh(M(1 - x_0)) - \sinh(M(1 - x)) \cosh(M x_0) + \sinh(M(1 - \min(x, x_0))) \cosh(M x_0) \right). \tag{35}$$

4 Results and Discussion

Substrate profiles and distributions produced by the model are first presented and discussed in Section 4.1 along with both experimental and numerical reference data from literature. The effect of substrate modulus and feed point number and placement on the substrate's volumetric variance were then calculated (Section 4.2). Instantaneous profiles of dissolved oxygen, temperature, pH, and carbon dioxide were estimated for the referenced large-scale experiments (Section 4.3). Finally, biomass yield effectivities were determined for the experimental references by first calculating oxygen uptake and adaptation efficiency factors directly from the experimental substrate concentration data (Section 4.4). The assumptions, limitations, and applicability of the model are evaluated in Section 4.5, and implications of the characterized profiles and distributions are discussed in Section 4.6.

4.1 Substrate profiles and distributions

As expected, the model predicts that the substrate concentration is always highest at the feed point and lowest furthest away from it (Supporting Information: Figure S2). At $M = 1$ the time-scales of mixing and reaction equal each other, but the substrate concentration is still quite homogeneous even when the feed is located at the slowest-to-mix points $x_0 = 1$ or $x_0 = 0$. In contrast, with $M = 4$ the heterogeneity of the reactor is considerable: the maximum concentration of substrate found at the feed point peaks at approximately two to four times the mean depending on the feed point placement, but a large fraction of the total volume has a concentration much lower than the mean. Instantaneous spatial profiles of substrate concentration produced by the model were compared against simulated profiles obtained with a complex metabolic model in a 2D compartment model (Pigou & Morchain, 2015) and also against *S. cerevisiae* fed-batch cultivations in an over 20 m^3 working volume (Larsson et al., 1996). Using the published parameters of the metabolic and hydrodynamic models, the substrate moduli M corresponding to the considered three profiles by Pigou and Morchain (2015) were estimated to be 1.46, 3.68, and 8.55 at 7 h, 9 h, and 15 h process times with 2.4 $g\,L^{-1}$, 5.0 $g\,L^{-1}$, and 14 $g\,L^{-1}$ biomass concentrations, respectively. The three profiles represented mild ($M = 1.46$) and severe ($M \geq 3.68$) mixing limitations with the time-scale of mixing being twice and over tenfold the time-scale of reaction. The profiles yielded by the linearized kinetics were in excellent agreement with the radially averaged profiles obtained by the much more complex modeling (Figure 1A). The volumetric feed rates and experimental substrate concentrations reported by Larsson et al. (1996) yielded substrate moduli ranging from 1.47 to 1.90. The biomass concentrations in these data were within 10 $g\,L^{-1}$–20 $g\,L^{-1}$. Their substrate profiles were relatively well represented by the model (Figure 1B), but the bottom-fed profiles were more homogeneous than the model estimated here.

According to the model, the distribution of substrate (Equations 10 and 11) is unimodal (i.e. has one distinct peak in density function) only if $x_0 \in \{0, 0.5, 1\}$ and bimodal otherwise (two peaks). One mode is always found at the minimum concentration, $u_{\min}$, and the possible second one always at u_{tres} when it differs from the maximum, $u_{\max}$. The distribution functions are not normal and they have more weight on concentrations lower than the mean (Supporting Information: Figure S3). The cumulative distribution functions of substrate concentration were calculated for the Pigou and Morchain (2015) data with the same substrate moduli as earlier (1.46, 3.68, and 8.55) but without radial averaging, and also for CFD-simulation results by Larsson et al. (1996), for which the substrate modulus was estimated to range from 3.0 to 4.4 using their kinetic parameters and operating conditions. The model produced almost identical distribution functions to Pigou and Morchain (2015) data (Figure 2A), but the Larsson et al. (1996) simulation data had higher variability than the model predicted (Figure 2B). Given the inevitable inaccuracy in estimating the CDF of the CFD-simulated substrate contour curves from Larsson et al. (1996), the model performed reasonably well (Figure 2B). The most notable discrepancies between the model here and the referenced simulations were found at the upper end of the substrate distributions, which was also expected due to the higher number of spatial dimensions in the cited works. The distribution functions of the referenced simulation data also appeared to increase in two stages, indicating bimodality of the substrate distribution. The bimodality is

interesting considering a previous modeling work where the heterogeneity of a large-scale reactor was modeled with a bimodal distribution of just two distinct concentration values, a high and a low one (Maluta et al., 2020).

The time-evolutions of local substrate concentrations were calculated with the model for the large-scale *S. cerevisiae* and *E. coli* fermentations with up to 40 h process times (Bylund et al., 1998; Larsson et al., 1996; Xu, Jahic, Blomsten, & Enfors, 1999). Error estimates (Section 2.4) were also calculated for the model fits. The top-fed run of the Bylund et al. (1998) large-scale experiments was not considered here, as the mean concentration of substrate could not be estimated owing to very high glucose concentrations measured at the top sampling port. The substrate modulus calculated with the reported volumetric feed rates and substrate concentrations ranged from 0.80 to 6.17 with a median of 3.9 and lower quartile of 3.0. In other words, most of the experimental data were estimated to have time-scales of mixing almost tenfold the time-scale of reaction or considerably more. The model fitted well the measured glucose concentrations of the over 20 m^3 *S. cerevisiae* fed-batches (Larsson et al., 1996) with top and bottom feeds. The batch with top feeding (Figure 3A) was fitted better than the bottom-fed batch (Figure 3B), where the measured heterogeneity was less than the model suggested here. Shown in Figures 3C and 3D, respectively, the large-scale *E. coli* fermentations were also well fitted by the model, but the bottom-fed 8 m^3 batch (Bylund et al., 1998) better than the 20 m^3 batch (Xu, Jahic, Blomsten, & Enfors, 1999), where the measurements showed less heterogeneity than the model. Altogether, approximately one half of the model values were within one estimated modeling error from the measured value (131/288). The logarithmic coefficient of determination was $Q^2 = 52\,\%$ with 2 % and 46 % contributions by systematic and random error, respectively, to fraction of variance unexplained. The distribution of logarithmic error was approximately normal (Supporting Information: Figure S4A). The conventional coefficient of determination was slightly higher at $R^2 = 62\,\%$, and the systematic error was negligible such that the fraction of variance unexplained (38 %) was solely due to random error in this metric based on absolute error. The distribution of residuals was rather symmetrical but sharper than normal, however (Supporting Information: Figure S4B).

The two coefficients of determinations were both above 50 % for the substrate time series data (Figure 3), which would be relatively low for a fitted correlation, but indicates good performance here as the model was not optimized to the data. Most of the uncertainty in model predictions was caused by the fact that the mean substrate concentration was not directly available but had to be estimated using only three experimental concentration values measured at the top, middle, and bottom of the reactors. The estimated mean values were on average 22 mg L^{-1} with a 21 mg L^{-1} standard deviation, which is reasonable for fed-batch operations, though. The uncertainty caused by diffusivity was small in comparison. The experimental values closest to the feed point were also rather variable, which was especially apparent with top feeds. Nevertheless, the error distributions showed good quality of fit in both absolute and relative error scales (Supporting Information: Figure S4). Most of the error was random and not systematic in nature, lack of precision instead of lack of accuracy.

4.2 Variance, substrate modulus, and feed points

Substrate's spatial variance was calculated as a function of substrate modulus with Equation 13 and also with experimental and numerical references (Larsson et al., 1996; Losoi et al., 2022; Pigou & Morchain, 2015) for comparison. According to the model, the variance starts eventually to grow linearly with respect to substrate modulus at higher values of M, which was somewhat apparent also in the experimental (Larsson et al., 1996) and numerical (Pigou & Morchain, 2015) references (Figure 4A). With a conventional top feed the substrate's volumetric standard deviation equals mean at $M \approx 4.0$ and half the mean at $M \approx 2.2$, where the time-scales of mixing are 16- and 4.8-fold the time-scale of reaction, respectively (Figure 4B). Interestingly, most of the experimental reference data (Larsson et al., 1996) with $x_0 = 0.88$ clustered around the model curve for simulation with $x_0 = 0.76$, and vice versa, the simulation reference data (Pigou & Morchain, 2015) seemed to follow the model curve for experiments. The higher-than-predicted variance of Pigou and Morchain (2015) data could be explained by the two-dimensionality and different kinetics of their simulation. The uncertainty in estimating the experimental substrate variance was high, as only three samples (top, middle, bottom) were available at each time point. The variances of the rest of the experimental substrate concentration data referenced earlier in this study were scattered quite randomly on the M,σ^2-plot (not shown). The effect of feed point placement and number demonstrated in a previous numerical work (Losoi et al., 2022) was reproduced by the simpler analytic modeling here: the variances were substantially lower with $x_0 = 0.5$ than with $x_0 = 1$ (equivalent to $x_0 = 0$) and practically null with symmetrical placement of two feed points at $x = 0.25$ and $x = 0.75$. The benefit of placing a single feed point in the middle instead of the top or bottom is also seen in Supporting Information: Figures S2B, S3B and S3D.

4.3 Profiles of DOT, temperature, pH, and CO_2

Just like the local concentration of substrate shows a peak around the feed point, the local concentration of dissolved oxygen sinks around the feed point and is higher in regions away from it. The heterogeneity of dissolved oxygen is coupled to the substrate's heterogeneity, which is defined by the feed point and substrate modulus (Supporting Information: Figure S5A). A lower transfer-to-demand ratio also lowers the overall level of dissolved oxygen (Supporting Information: Figure S5B) and exacerbates the oxygen limitation around the feed point. Figure 5A shows DOT profiles estimated for the experimental references at time points corresponding to $20\,\mathrm{g\,L^{-1}}$ biomass concentrations and a constant feed (parameters in Table 1). The substrate modulus was estimated to be between 4.1 and 5.5 using the reported volumetric feed rates and mean concentrations. The proportion of oxygen-limited zones (DOT = 0 with the zeroth-order kinetic approximation) was calculated to be 22 %–46 % (Equation 17). The bottom-fed cultivations showed less limitation due to higher hydrostatic pressure at the feed point where the local oxygen demand was highest. The works referenced here did not include spatial profiles of dissolved oxygen, and as such, direct comparison was not possible. Oxygen limitations were not detected in any of the referenced works directly with the probes at the middle of the reactors. However, Bylund et al. (1998) hypothesized that oxygen

limitations could have occurred around the feed points in their experiments, and likewise Xu, Jahic, Blomsten, and Enfors (1999) estimated based on the formate accumulation that approximately 12 % of the culture volume would have been anoxic. The modeling performed here was in accordance with these hypotheses: a poorly-mixing substrate feed might localize the oxygen demand such that the limitation is undetected by the electrode(s) just as suggested in literature (Figure 5A, Supporting Information: Figure S5A).

The axial profile of temperature is similar to the dissolved oxygen profile in that its shape is defined by the substrate profile and its two parameters, the feed point and substrate modulus (Supporting Information: Figure S6). However, the temperature profile is not as sharp as the oxygen profile, but much smoother. The temperature modulus (Equation 30) defines the magnitude of the distribution. Figure 5B shows temperature profiles estimated for the experimental references (Table 1) corresponding to the same time instants as in Figure 5A with DOT profile estimates. The oxygen uptake efficiencies were estimated to be 57 %–85 % in these situations, leading to $0.83\,\mathrm{g\,L^{-1}\,h^{-1}}$–$1.55\,\mathrm{g\,L^{-1}\,h^{-1}}$ oxygen uptake rates. Consequently, the maximal gas-phase oxygen conversions would have been 8 %–13 %. The axial temperature differences within the reactors were then estimated to be 0.04 °C–0.12 °C. Based on the modeling here, the axial profile of temperature should have been virtually homogeneous in the axial dimension in the referenced large-scale experiments. With a higher $1\,\mathrm{g\,g^{-1}}$ consumption of oxygen per substrate the estimated temperature differences would have been only up to 0.16 °C, which is still negligible. For a general assessment of whether axial temperature differences could be expected to occur, temperature differences were evaluated with substrate feed rate and 95 % mixing time as parameters by assuming $\langle S \rangle = 0.05\,\mathrm{g\,L^{-1}}$, $x_0 = 1$, and OUR = ODR = $0.446 Q_S$. According to these estimates a notable temperature difference of 1 °C-scale could occur at large scale ($t_{95} \geq 100\,\mathrm{s}$) with approximately $10\,\mathrm{g\,L^{-1}\,h^{-1}}$ substrate feed rates or higher, provided that oxygen transfer is not limiting (Table 4). Again, a higher than $0.446\,\mathrm{g\,g^{-1}}$ consumption of oxygen per substrate would increase the difference accordingly. No reports of axial temperature differences were found in experimental literature, and no simulation works were found either, which implies that either there is no reason to expect any major axial differences to exist or they have been neglected. The estimations for axial temperature differences in the referenced experiments were very small, which strongly suggests the former. Unless $10\,\mathrm{g\,L^{-1}\,h^{-1}}$ substrate feed rates are utilized with sufficient oxygen transfer (Table 4), the assumption of axially constant temperature remains applicable. Local temperature differences in the proximity of the heat transfer surfaces are more likely to exist.

Similarly to the earlier profiles, the pH profiles are also sharp at the feed point and the heterogeneity can be decreased by injecting the pH correcting agent into the middle instead of the top or bottom (Supporting Information: Figure S7A). Higher addition rates of the pH correcting agent resulted in higher variability in the axial pH profile (Supporting Information: Figure S7B). The location of the medium's $\mathrm{p}K_\mathrm{a}$ in relation to the control value had a minor effect (Supporting Information: Figure S7C). It was also observed that the higher the control treshold around the pH control value, the higher the expected heterogeneity at the end of the control cycle (Supporting Information: Figure S7D). Bylund et al. (1998) and Xu, Jahic, Blomsten, and Enfors (1999) both used a 25 % NH_4OH solution added at the top of the reactor to maintain pH at 7 during their large-scale *E. coli* fed-batches. Coincidentally the

pH modulus (Equation 33) was practically equal for both cases when assuming that the volume flow rate of the alkalic solution during pH control cycles was the same as the volume flow of the substrate solution. Since the exact flow rate of the pH-dosing pumps was not known here, cases with 0.5-, 2, and 4-fold flow rates were also considered for comparison. According to the modeling here, long-term heterogeneity in axial pH profiles cannot be ruled out: pH differences of up to 0.06, 0.11, and 0.22 were estimated with the same volume flow rate as with substrate ($M_{\mathrm{pH}} = 0.59$) and with 2- and 4-fold flow rates ($M_{\mathrm{pH}} = 1.18$ and $M_{\mathrm{pH}} = 2.37$), respectively (Figure 6). During the initial transients at the beginning of pH adjustment, when the steady-state approximation is not yet valid, larger differences close to the dosing point of acids or alkali would be expected. For comparison, Langheinrich and Nienow (1999) measured an excess of 0.6 units at the top during the addition of an alkaline solution in a 8 m^3 working volume reactor.

The profile of $p_{\mathrm{CO_2}}$ was different from the others in that it was modeled by plug-flow without any dispersion. Consequently, the partial pressure was always zero at the bottom (Supporting Information: Figure S8A). Like the temperature profile, the CO_2 profile was not as sharp as the substrate, DOT, or pH profiles. The effect of the heterogeneity in substrate, or CO_2 release, profile depended on the feed point's location: increased heterogeneity of substrate correlated negatively with mean CO_2 when $x_0 > 0.5$ but positively when $x_0 < 0.5$ (Supporting Information: Figure S8B). According to the $p_{\mathrm{CO_2}}$-profiles estimated for the experimental references (Bylund et al., 1998; Larsson et al., 1996; Xu, Jahic, Blomsten, & Enfors, 1999), the mean $p_{\mathrm{CO_2}}$ may have been relatively low, mostly below 50 mbar, when top feeds were utilized (Figure 5C). Bottom feeds increased the gas-phase CO_2 content earlier on, and $p_{\mathrm{CO_2}} \geq 150$ mbar was estimated in majority of Bylund et al. (1998) bottom-fed case. The outlet partial pressures were estimated to 69 mbar–165 mbar assuming total oxidation of glucose. The CO_2-profiles were plausible: Baez et al. (2009) measured 110 mbar dissolved CO_2 at a 5 L reactor with 60 g L^{-1} *E. coli*. It was suggested by Baez et al. (2009) that the CO_2 pressure might increase up to 300 mbar at the bottom of a large reactor due to hydrostatic pressure. The modeling performed suggests that in a fed-batch process such high values are obtainable at the bottom only if the feed is at the bottom as well. The neglect of gas-phase dispersion influenced the model in this respect.

4.4 Efficiency factors

The experimental data referenced above in Section 4.1 were also used to estimate time-averaged efficiency factors for the experiments. Both the oxygen uptake and adaptation efficiency factors (Equations 21 and 24) were calculated for the same reported time points as in Figures 3C and 3D using the same substrate moduli calculated from the reported volumetric feed rates and substrate concentrations. In comparison with small scale, Xu, Jahic, Blomsten, and Enfors (1999) reported a $0.31/0.41 \approx 76$ % yield efficiency in large scale during the constant-feed phase. Time-averaged yield efficiencies of 88 % and 86 % were estimated here by oxygen uptake and adaptation efficiencies of 83 % and 70 %, respectively, resulting in a total yield effectivity of $0.88 \times 0.86 = 75$ %. Bylund et al. (1998) reported a 85.5 % biomass in their bottom-fed large-scale *E. coli* batch in comparison with a small-scale batch, and here the estimated time-averaged yield effectivities were 82 % based on estimated oxygen uptake efficiency of 74 % and 84 % based on

adaptation efficiency of 67 %. Larsson et al. (1996) did not report comparisons of lab- and large-scale yields. In general, the efficiency factors of both adaptation and oxygen uptake decrease as substrate modulus and heterogeneity increase, and the better-homogenized middle feed retains fair efficiencies even with a considerably high substrate modulus of $M = 4$ (Supporting Information: Figures S9A and S9B). Furthermore, the positive effect of hydrostatic pressure on oxygen transfer is lost with a top feed as substrate heterogeneity increases and local oxygen demand localizes (Supporting Information: Figures S9C and S9D). From the perspective of oxygen transfer, a bottom feed can even outperform the better-mixing middle feed if the hydrostatic pressure at the bottom is comparable to the head-space pressure (Supporting Information: Figure S9D).

Even though the efficiency factors were rather simplistic, they were consistent with the yields reported in literature. Estimation of the time-averaged η_{OUR} for Bylund et al. (1998) experiments was rather uncertain, though. Both the gas flow rate and stirrer rate were adjusted in their experiments, but here just the middle point of the range was assumed to hold for the entire duration. The oxygen transfer rate coefficient was also only roughly approximated from other experiments. Also the time-averaged OUR-effectivities were estimated using a time-independent coefficient of oxygen consumption per substrate, even though the consumption is likely to increase during a fed-batch process (Bylund et al., 2000). Furthermore, the yield losses estimated here were simplified also that the sense that the effect of maintenance was not considered. Interestingly, Maluta et al. (2020) correlated yield loss to substrate variance. Here, the simple yield losses were also related to variance through both the population balance concept but also through oxygen uptake efficiency. The relation was not linear, though, unlike in their modeling work.

4.5 Assumptions, limitations, and applicability of the model

First, it should be noted that the model was not optimized to any of the experimental or numerical references, but the diffusivities were calculated directly from operating conditions using the methodology developed in Part I of this study (Losoi et al., 2023), and the kinetic parameters and mean concentrations were obtained or calculated from the referenced works. The model involved two main assumptions on the kinetics: (1) The substrate consumption was considered to be linear or first-order with respect to substrate concentration. (2) The rest of the consumption or production rates were modeled with zeroth-order kinetics by first estimating the overall volumetric rate using a global balance and then using the substrate profile to transform this total consumption or production rate to a local rate. Hydrodynamically the major assumptions were to assume (1) turbulent axial dispersion for the liquid phase and (2) plug flow for the gas phase. The solid phase (biomass) was not distinguished from the liquid phase here.

The assumption of linear substrate consumption rate might seem unlogical, as Monod kinetics are almost invariably used in bioreactor modeling studies. However, the linearized consumption rate yielded similar substrate profiles in the 1D diffusion equation's context as regular Monod kinetics (Supporting Information: Figure S1). Furthermore, it has been pointed out previously that Monod kinetics have been validated in homogeneous conditions in chemostat and batch cultivations, where the cell population has adapted to its environment (Morchain & Fonade, 2009; Morchain et al., 2013). Scale-down experiments have shown that the Monod kinetics do not apply at dynamic,

heterogeneous conditions (Xu, Jahic, Blomsten, & Enfors, 1999): substrate uptake rates exceeding the "maximal rate" parameter have been found, when a culture is suddenly exposed to a higher substrate concentration than what it has adapted to. Thus, the linearized kinetics are actually more realistic than the standard Monod kinetics in that they allow the uptake rate to exceed the conventional maximal uptake rate. The linearization with substrate mean concentration also simplifies to standard Monod kinetics in homogeneous conditions.

Using the substrate profile to estimate the local consumption or production rates from a global volumetric rate was a convenient choice that allowed analytical profiles to be formed for dissolved oxygen, temperature, and CO_2. This implied a one-way coupling between substrate and oxygen and substrate and CO_2: substrate induced oxygen consumption and CO_2 release, but their availability or presence did not influence substrate consumption. A two-way coupling would be more appropriate, but in a fed-batch context the overall substrate consumption rate eventually equals the volumetric feed rate, making the straightforward one-way coupling more applicable. In a batch reactor the two-way coupling would be more critical. The zeroth-order oxygen consumption simplified the treatment substantially, as it also allowed discarding the standard Monod parameters of oxygen consumption, requiring only the estimated overall oxygen demand rate and transfer rate coefficient. The obtained oxygen profiles were more indicative of potential oxygen limitation zones that could be defined here as environments with $O_{\mathrm{L}} = 0$, but probably less applicable as definitive profiles. There is always some upper limit to biological oxidative capacity (Szenk et al., 2017), which was not considered in this modeling work, however. It would be possible to estimate the spatial profile of dissolved oxygen using also a biological limit to local uptake rate. This would hardly bring substantial value, when the objective is simply to detect potential oxygen limitation around feed points in a fed-batch. Deriving oxygen uptake effectivity would also be complicated after adding such a biological limit. In a batch setting the biomass-specific rates and limits to them play a more important role, when the oxygen consumption is not as limited by substrate availability. Likewise the profiles of temperature and CO_2 were relatively easy to obtain using the substrate profile. For simplicity, local limitations in oxygen transfer were not considered in determining the temperature profile. Instead, the local limitations were incorporated through the oxygen uptake efficiency factor η_{OUR}, which affected the overall oxygen consumption and heat release rate. Using a nonuniform cooling in obtaining the temperature would have affected the profile, but most likely not in a significant amount.

The zeroth-order pH profile approximation gave a quick view to potential pH gradients during pH control. The steady-state methodology does not apply to the initial transient. The profiles are most applicable between correction cycle middle and end when the initial transient has smoothed out.

As for the hydrodynamic assumptions, the use of turbulent dispersion for the liquid phase was treated and validated in Part I of this study (Losoi et al., 2023). Plug flow assumption for the gas phase was necessary here to obtain an estimate of CO_2 profiles. The assumption could be considered reasonable in the high aspect ratio reactors studied here. With lower aspect ratios it is probable that axial dispersion cannot be neglected. Its use also implied that the liquid phase is locally saturated with CO_2 such that all produced CO_2 is released as gas and none dissolves.

A high oxygen flow rate was necessary for assuming undepleted gas-phase. With lower flow rates relative to

theoretical maximum consumption the gas-phase conversion should be taken into account. However, this would complicate the efficiency factor calculations. For preliminary analyses it is perhaps easiest to use zero conversion and to note that if limitations are predicted, they are likely to occur as well. In the modeling performed here, the assumption of negligible gas-phase conversion of oxygen was not too bold. In some other context, using zero conversion throughout would be unreasonable. If non-zero conversion cannot be assumed, the profile of gas-phase oxygen could be roughly estimated similarly to CO_2 by a plug flow equation but with spatially dependent consumption. The axial and radial differences in oxygen transfer rate coefficients due to impeller vicinity (Oosterhuis & Kossen, 1984) were neglected for simplicity. In a heterogeneous fed-batch setting such as here the spatial variations in $k_L a$ are not necessarily as important as in a homogeneous batch setting, where the oxygen demand by substrate is more-or-less uniform across the whole reactor. It would be possible to use a spatially heterogeneous transfer rate coefficient for oxygen when estimating the profiles, if more precise data were available, or by correlations (Oosterhuis & Kossen, 1984). Also, the space below the sparger at the bottom can usually be expected to be poorly oxygenated (Oosterhuis & Kossen, 1984), which was not accounted for here.

4.6 Implications

With over $40\,\mathrm{g\,L^{-1}}$ biomass concentrations or $16\,\mathrm{g\,L^{-1}\,h^{-1}}$ feed rates, mixing limitations ($M > 1$) begin to occur even with only $t_{95} = 10\,\mathrm{s}$ mixing times characteristic to small-scale equipment. In large-scale reactors, where $t_{95} > 200\,\mathrm{s}$ and longer mixing times are possible, mixing limitations may appear already with low biomass concentrations of $5\,\mathrm{g\,L^{-1}}$ or feed rates of $1\,\mathrm{g\,L^{-1}\,h^{-1}}$ (Tables 2 and 3). Heterogeneous substrate concentration profiles localize oxygen demand as well, leading to anoxic zones. Similarly the use of cofeeding strategies, where an additional high-energy substrate is supplied in low concentrations (Park et al., 2019), could be compromized by the high substrate concentrations found near the feeding points. If the substrate feed rates were more intensive, e.g. $10\,\mathrm{g\,L^{-1}\,h^{-1}}$, and oxygen transfer were not limiting, measurable axial temperature differences might be expected.

Based on the various negative effects of the characterized heterogeneity, it is suggested that large-scale reactors should be homogenized more effectively. Of all the alternatives, the use of multiple feed points or at least positioning the feed at the middle instead of at the top (Losoi et al., 2022) could be the easiest to implement. Symmetrical feed placement divides the effective working height by the number of feed points N such that $M \sim N^{-1}$, $M_T \sim N^{-2}$, and $M_{\mathrm{pH}} \sim N^{-2}$, leading to a quick decrease in the time-scale of mixing and heterogeneity. Homogeneity in gas phase is not achievable by feed arrangements, but linear gas-phase composition profiles would be found in case of a homogeneous liquid phase. For pH control it can be suggested that a minimal volume flow rate should be used together with relatively tight control thresholds to avoid persisting pH gradients in the reactor.

5 Conclusions

The aim of this two-part study was to comprehensively model large-scale stirred bioreactors using 1D diffusion equations. Part I of this study (Losoi et al., 2023) presented a computation formula for the model's parameter, the axial diffusivity, and validated it against a large set of previously published experimental data. This second part employed the model to characterize substrate, pH, oxygen, CO_2, and temperature profiles with few dimensionless numbers in typical fed-batch contexts. The characterizations were compared with available experimental and numerical data, and good accordance was found even though the model was not optimized to the reference data. The modeling suggested that indeed each of the five variables could be heterogeneous, though pH and temperature not as severely as substrate and oxygen. According to the model, appropriate feed point placement could effectively homogenize the liquid phase. CO_2 could not be homogenized in a tall reactor, but a linear profile of gas-phase content could be expected if the reactor were homogeneous. Likewise, gas-phase O_2 conversion would be expected to be linear in a tall but homogeneous reactor. Based on this two-part study, 1D diffusion equations can be applied for simple and predictive preliminary modeling of typical large-scale stirred bioreactors.

Author contributions

Pauli Losoi developed the model, performed the computations and analysis, and wrote the manuscript. Jukka Konttinen and Ville Santala supervised the study and revised the manuscript.

Acknowledgements

Financial support by Tampere University of Technology Graduate School is acknowledged. The work presented in this article is supported by Novo Nordisk Foundation grant NNF22OC0079579.

Conflict of interest

The authors declare that there are no conflicts of interest.

Data availability

The data that support the findings of this study are available from the corresponding author upon reasonable request.

Supporting information

Supplementary Text: Figures S1–S9.

References

Baez, A., Flores, N., Bolívar, F., & Ramírez, O. T. (2009). Metabolic and transcriptional response of recombinant *Escherichia coli* to elevated dissolved carbon dioxide concentrations. *Biotechnology and Bioengineering*, *104*(1), 102–110. https://doi.org/10.1002/bit.22379

Bisgaard, J., Zahn, J. A., Tajsoleiman, T., Rasmussen, T., Huusom, J. K., & Gernaey, K. V. (2022). Data-based dynamic compartment model: Modeling of *E. coli* fed-batch fermentation in a 600 m^3 bubble column. *Journal of Industrial Microbiology and Biotechnology*, *49*(5). https://doi.org/10.1093/jimb/kuac021

Bylund, F., Castan, A., Mikkola, R., Veide, A., & Larsson, G. (2000). Influence of scale-up on the quality of recombinant human growth hormone. *Biotechnology and Bioengineering*, *69*(2), 119–128. https://doi.org/10.1002/(SICI)1097-0290(20000720)69:2⟨119::AID-BIT1⟩3.0.CO;2-9

Bylund, F., Collet, E., Enfors, S., & Larsson, G. (1998). Substrate gradient formation in the large-scale bioreactor lowers cell yield and increases by-product formation. *Bioprocess Engineering*, *18*, 171–180. https://doi.org/10.1007/s004490050427

Caspeta, L., Flores, N., Pérez, N. O., Bolívar, F., & Ramírez, O. T. (2009). The effect of heating rate on *Escherichia coli* metabolism, physiological stress, transcriptional response, and production of temperature-induced recombinant protein: A scale-down study. *Biotechnology and Bioengineering*, *102*(2), 468–482. https://doi.org/10.1002/bit.22084

Castan, A., & Enfors, S. (2002). Formate accumulation due to DNA release in aerobic cultivations of *Escherichia coli*. *Biotechnology and Bioengineering*, *77*, 324–328. https://doi.org/10.1002/bit.1198

Cole, K. D., Beck, J. V., Haji-Sheikh, A., & Litkouhi, B. (2010). *Heat conduction using Green's functions* (2nd ed.). CRC Press. https://doi.org/10.1201/9781439895214

Delvigne, F., El Mejdoub, T., Destain, J., Delroisse, J.-M., Vandenbol, M., Haubruge, E., & Thonart, P. (2005). Estimation of bioreactor efficiency through structured hydrodynamic modeling case study of a *Pichia pastoris* fed-batch process. *Applied Biochemistry and Biotechnology*, *122*, 653–671. https://doi.org/10.1385/ABAB:122:1-3:0653

Doran, P. M. (2013). *Bioprocess engineering principles* (2nd ed.). Academic Press. https://doi.org/10.1016/C2009-0-22348-8

Enfors, S., Jahic, M., Rozkov, A., Xu, B., Hecker, M., Jürgen, B., Krüger, E., Schweder, T., Hamer, G., O'Beirne, D., Noisommit-Rizzi, N., Reuss, M., Boone, L., Hewitt, C., McFarlane, C., Nienow, A., Kovacs, T., Trägårdh, C., Fuchs, L., … Manelius, Å. (2001). Physiological responses to mixing in large scale bioreactors. *Journal of Biotechnology*, *85*, 175–185. https://doi.org/10.1016/S0168-1656(00)00365-5

Gabelle, J., Augier, F., Carvalho, A., Rousset, R., & Morchain, J. (2011). Effect of tank size on $k_L a$ and mixing time in aerated stirred reactors with non-Newtonian fluids. *The Canadian Journal of Chemical Engineering*, *89*, 1139–1153. https://doi.org/10.1002/cjce.20571

Haringa, C., Tang, W., Wang, G., Deshmukh, A. T., van Winden, W. A., Chu, J., van Gulik, W. M., Heijnen, J. J., Mudde, R. F., & Noorman, H. J. (2018). Computational fluid dynamics simulation of an industrial *P. chrysogenum* fermentation with a coupled 9-pool metabolic model: Towards rational scale-down and design optimization. *Chemical Engineering Science*, *175*, 12–24. https://doi.org/10.1016/j.ces.2017.09.020

Harris, C. R., Millman, K. J., van der Walt, S. J., Gommers, R., Virtanen, P., Cournapeau, D., Wieser, E., Taylor, J., Berg, S., Smith, N. J., Kern, R., Picus, M., Hoyer, S., van Kerkwijk, M. H., Brett, M., Haldane, A., Fernández del Río, J., Wiebe, M., Peterson, P., … Oliphant, T. E. (2020). Array programming with NumPy. *Nature*, *585*, 357–362. https://doi.org/10.1038/s41586-020-2649-2

Kawase, Y., & Moo-Young, M. (1989). Mixing time in bioreactors. *Journal of Chemical Technology and Biotechnology*, *44*, 63–75. https://doi.org/10.1002/jctb.280440107

Langheinrich, C., & Nienow, A. W. (1999). Control of pH in large-scale, free suspension animal cell bioreactors: Alkali addition and pH excursions. *Biotechnology and Bioengineering*, *66*(3), 171–179. https://doi.org/10.1002/(SICI)1097-0290(1999)66:3⟨171::AID-BIT5⟩3.0.CO;2-T

Larsson, G., Törnkvist, M., Ståhl-Wernersson, E., Trägårdh, C., Noorman, H., & Enfors, S. (1996). Substrate gradients in bioreactors: Origin and consequences. *Bioprocess Engineering*, *14*, 281–289. https://doi.org/10.1007/BF00369471

Losoi, P., Konttinen, J., & Santala, V. (2022). Substantial gradient mitigation in simulated large-scale bioreactors by optimally placed multiple feed points. *Biotechnology and Bioengineering*, *119*(12), 3549–3566. https://doi.org/10.1002/bit.28232

Losoi, P., Konttinen, J., & Santala, V. (2023). Modeling large-scale bioreactors with diffusion equations. Part I: Predicting axial diffusivity and mixing times. *Submitted to Biotechnology and Bioengineering*.

Machon, V., & Jahoda, M. (2000). Liquid homogenization in aerated multi-impeller stirred vessel. *Chemical Engineering and Technology*, *23*, 869–876. https://doi.org/10.1002/1521-4125(200010)23:10⟨869::AID-CEAT869⟩3.0.CO;2-B

Maluta, F., Pigou, M., Montante, G., & Morchain, J. (2020). Modeling the effects of substrate fluctuations on the maintenance rate in bioreactors with a probabilistic approach. *Biochemical Engineering Journal*, *157*, 107536. https://doi.org/10.1016/j.bej.2020.107536

McKinney, W. (2010). Data structures for statistical computing in Python. *Proceedings of the 9th Python in Science Conference*, 51–56. https://doi.org/10.25080/Majora-92bf1922-00a

Meurer, A., Smith, C. P., Paprocki, M., Čertík, O., Kirpichev, S. B., Rocklin, M., Kumar, A., Ivanov, S., Moore, J. K., Singh, S., Rathnayake, T., Vig, S., Granger, B. E., Muller, R. P., Bonazzi, F., Gupta, H., Vats, S., Johansson, F., Pedregosa, F., … Scopatz, A. (2017). SymPy: Symbolic computing in Python. *PeerJ Computer Science*, *3*, e103. https://doi.org/10.7717/peerj-cs.103

Morchain, J., & Fonade, C. (2009). A structured model for the simulation of bioreactors under transient conditions. *AIChE Journal*, *55*(11), 2973–2984. https://doi.org/10.1002/aic.11906

Morchain, J., Gabelle, J., & Cockx, A. (2013). A coupling of biokinetic and population balance models to account for biologial heterogeneity in bioreactors. *AIChE Journal*, *59*(2), 369–379. https://doi.org/10.1002/aic.13820

Morchain, J., Gabelle, J., & Cockx, A. (2014). A coupled population balance model and CFD approach for the simulation of mixing issues in lab-scale and industrial bioreactors. *AIChE Journal*, *60*(1), 27–40. https://doi.org/10.1002/aic.14238

Nadal-Rey, G., McClure, D. D., Kavanagh, J. M., Cornelissen, S., Fletcher, D. F., & Gernaey, K. V. (2021). Understanding gradients in industrial bioreactors. *Biotechnology Advances*, (107660), 107660. https://doi.org/10.1016/j.biotechadv.2020.107660

Neubauer, P., & Junne, S. (2010). Scale-down simulators for metabolic analysis of large-scale bioprocesses. *Current Opinion in Biotechnology*, *21*, 114–121. https://doi.org/10.1016/j.copbio.2010.02.001

Oosterhuis, N. M. G., & Kossen, N. W. F. (1984). Dissolved oxygen concentration profiles in a production-scale bioreactor. *Biotechnology and Bioengineering*, *26*(5), 546–550. https://doi.org/10.1002/bit.260260522

Park, J. O., Liu, N., Holinski, K. M., Emerson, D. F., Qiao, K., Woolston, B. M., Xu, J., Lazar, Z., Islam, M. A., Vidoudez, C., Girguis, P. R., & Stephanopoulos, G. (2019). Synergistic substrate cofeeding stimulates reductive metabolism. *Nature Metabolism*, *1*, 643–651. https://doi.org/10.1038/s42255-019-0077-0

Pigou, M., & Morchain, J. (2015). Investigating the interactions between physical and biological heterogeneities in bioreactors using compartment, population balance and metabolic models. *Chemical Engineering Science*, *126*, 267–282. https://doi.org/10.1016/j.ces.2014.11.035

Pinelli, D., & Magelli, F. (2000). Analysis of the fluid dynamic behavior of the liquid and gas phases in reactors stirred with multiple hydrofoil impellers. *Industrial & Engineering Chemistry Research*, *39*(9), 3202–3211. https://doi.org/10.1021/ie000216+

Risager Wright, N., Rønnest, N. P., & Thykaer, J. (2016). Scale-down of continuous protein producing *Saccharomyces cerevisiae* cultivations using a two-compartment system. *Biotechnology Progress*, *32*(1), 152–159. https://doi.org/10.1002/btpr.2184

Rohatgi, A. (2020). Webplotdigitizer: Version 4.4. https://automeris.io/WebPlotDigitizer

Rumble, J. R. (Ed.). (2022). *CRC Handbook of Chemistry and Physics* (103rd ed.). CRC Press/Taylor & Francis. Internet Version.

Sander, R. (2015). Compilation of Henry's law constants (version 4.0) for water as solvent. *Atmospheric Chemistry and Physics*, *15*, 4399–4981. https://doi.org/10.5194/acp-15-4399-2015

Schweder, T., Krüger, E., Xu, B., Jürgen, B., Blomsten, G., Enfors, S.-O., & Hecker, M. (1999). Monitoring of genes that respond to process-related stress in large-scale bioprocesses. *Biotechnology and Bioengineering*, *65*(2), 151–159. https://doi.org/10.1002/(SICI)1097-0290(19991020)65:2⟨151::AID-BIT4⟩3.0.CO;2-V

Szenk, M., Dill, K. A., & de Graff, A. M. R. (2017). Why do fast-growing bacteria enter overflow metabolism? Testing the membrane real estate hypothesis. *Cell Systems*, *5*, 95–104. https://doi.org/10.1016/j.cels.2017.06.005

The pandas development team. (2020). *Pandas* (Version 1.1.3). Zenodo. https://doi.org/10.5281/zenodo.4067057

Virtanen, P., Gommers, R., Oliphant, T. E., Haberland, M., Reddy, T., Cournapeau, D., Burovski, E., Peterson, P., Weckesser, W., Bright, J., van der Walt, S. J., Brett, M., Wilson, J., Millman, K. J., Mayorov, N., Nelson, A. R. J., Jones, E., Kern, R., Larson, E., . . . SciPy 1.0 Contributors. (2020). SciPy 1.0: Fundamental algorithms for scientific computing in Python. *Nature Methods*, *17*, 261–272. https://doi.org/10.1038/s41592-019-0686-2

Vrábel, P., van der Lans, R. G. J. M., Cui, Y. Q., & Luyben, K. C. A. M. (1999). Compartment model approach: Mixing in large scale aerated reactors with multiple impellers. *Chemical Engineering Research and Design*, *77*, 291–302. https://doi.org/10.1205/026387699526223

Vrábel, P., van der Lans, R. G. J. M., Luyben, K. C. A. M., Boon, L., & Nienow, A. W. (2000). Mixing in large-scale vessels stirred with multiple radial or radial and axial up-pumping impellers: Modelling and measurements. *Chemical Engineering Science*, *55*, 5881–5896. https://doi.org/10.1016/S0009-2509(00)00175-5

Vrábel, P., van der Lans, R. G. J. M., van der Schot, F. N., Luyben, K. C. A. M., Xu, B., & Enfors, S. (2001). CMA: Integration of fluid dynamics and microbial kinetics in modelling of large-scale fermentations. *Chemical Engineering Journal*, *84*, 463–474. https://doi.org/10.1016/S1385-8947(00)00271-0

Xu, B., Jahic, M., Blomsten, G., & Enfors, S. (1999). Glucose overflow metabolism and mixed-acid fermentation in aerobic large-scale fed-batch processes with *Escherichia coli*. *Applied Microbiology and Biotechnology*, *51*, 564–571. https://doi.org/10.1007/s002530051433

Xu, B., Jahic, M., & Enfors, S. (1999). Modeling of Overflow Metabolism in Batch and Fed-Batch Cultures of *Escherichia coli*. *Biotechnology Progress*, *15*, 81–90. https://doi.org/10.1021/bp9801087

Tables

Table 1: Referenced large-scale experiments.

Quantity	Unit	L96	B98	X99
V_L	m^3	20.8 (t) / 19.8 (b)	8.0	22.4
ϵ_G	%	17.1	13.1 (correlated)	17.5
H	m	7.3 (t) / 7.0 (b)	3.5	7.9
n	rpm	133	113 (75–150)	133
v_G/V_L	vvm	0.525 (t) / 0.552 (b)	0.50 (0.25–0.75)	0.48
d	$m^2\,s^{-1}$	0.126 (t) / 0.121 (b)	0.094	0.134
t_{95}	s	159 (t) / 149 (b)	49	175
Q_S	$g\,L^{-1}\,h^{-1}$	2.58 (t) / 2.72 (b)	5.9	3.86
$\langle S \rangle$	$mg\,L^{-1}$	10	10	30
q_S	$g\,g^{-1}\,h^{-1}$	1.7	1.35	1.35
K_S	$g\,L^{-1}$	0.18	0.05	0.05
Reference		Larsson et al. (1996)	Bylund et al. (1998)	Xu, Jahic, Blomsten, and Enfors (1999)

Symbols: V_L, liquid volume; ϵ_G, overall gas holdup; H, overall dispersion height; n, stirrer rate; v_G/V_L, volume flow of gas per liquid volume; d, axial diffusivity; t_{95}, longest possible 95 % mixing time; Q_S, volumetric substrate feed rate during constant-feed phase; $\langle S \rangle$, estimated mean substrate concentration during constant-feed phase at $20\,g\,L^{-1}$ biomass concentration; q_S, specific substrate consumption rate; K_S, Monod constant for substrate consumption.
Notes: The diffusivities and mixing times were calculated as in Part I of this study (Losoi et al., 2023) based on the operating conditions reported in the references. Larsson et al. (1996) reported the specific substrate consumption rate and Monod constant, and values reported in Xu, Jahic, and Enfors (1999) were used for Bylund et al. (1998) and Xu, Jahic, Blomsten, and Enfors (1999). Larsson et al. (1996) conducted two experiments, one with the feed at the top (t) and the other with the feed at the bottom (b). Bylund et al. (1998) reported ranges of values for stirrer and gas flow rates (shown in parentheses here), and their means were used.

Table 2: Example values for kinetically calculated substrate modulus $M \approx 0.0862\sqrt{(X/g\,L^{-1})(t_{95}/s)}$.

X / $g\,L^{-1}$	t_{95} = 10 s	t_{95} = 100 s	t_{95} = 200 s
1	0.27	0.86	1.22
5	0.61	1.93	2.73
10	0.86	2.73	3.86
20	1.22	3.86	5.45
40	1.72	5.45	7.71

Symbols: M, substrate modulus (Equation 7); X, biomass concentration; t_{95}, 95 % mixing time with widest possible feed-probe distance.

Table 3: Example values substrate modulus with feed-based calculation $M \approx 0.122\sqrt{(Q_S/g\,L^{-1}\,h^{-1})(t_{95}/s)}$.

Q_S / $g\,L^{-1}\,h^{-1}$	t_{95} = 10 s	t_{95} = 100 s	t_{95} = 200 s
1	0.39	1.22	1.72
2	0.55	1.72	2.44
4	0.77	2.44	3.45
8	1.09	3.45	4.88
16	1.54	4.88	6.90

Symbols: M, substrate modulus (Equation 8); Q_S, volumetric feed rate of substrate; t_{95}, 95 % mixing time with widest possible feed-probe distance.

Table 4: Axial temperature differences (°C) between top and bottom evaluated with different substrate feed rates Q_S and 95 % mixing times assuming $\langle S \rangle = 0.05\,\mathrm{g\,L^{-1}}$, $x_0 = 1$, and OUR = ODR = $0.446 Q_S$.

$Q_S/\mathrm{g\,L^{-1}\,h^{-1}}$	$t_{95} = 10\,\mathrm{s}$	$t_{95} = 100\,\mathrm{s}$	$t_{95} = 200\,\mathrm{s}$
1	0.00	0.01	0.05
2	0.00	0.05	0.16
4	0.00	0.16	0.47
8	0.01	0.47	1.22
16	0.03	1.22	2.91

Symbols: Q_S, volumetric feed rate of substrate; t_{95}, 95 % mixing time with widest possible feed-probe distance.

List of Figures

Figures

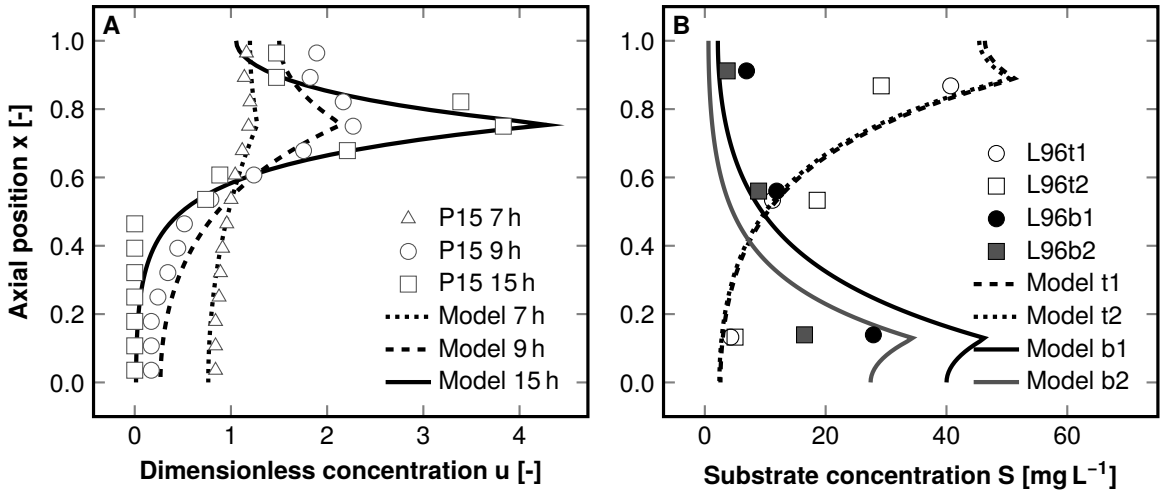

Figure 1: Axial profile of dimensionless substrate concentration. (A) The marks show data obtained from a numerical study by Pigou and Morchain (2015). (B) Experimental data by Larsson et al. (1996), top (t) and bottom (b) feeds, biomass concentrations 10, 15, 10, 20 (g L^{-1}).

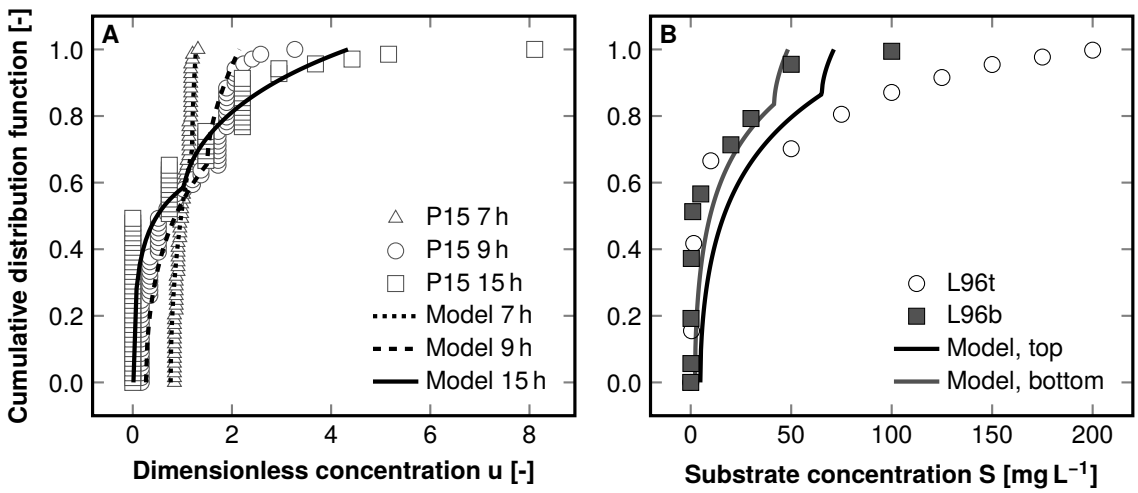

Figure 2: Substrate concentration's cumulative distribution functions. (A) The marks show data obtained from a numerical study by Pigou and Morchain (2015). (B) Simulation data by Larsson et al. (1996) with top (t) and bottom feeds (b). Biomass concentrations 15 g L^{-1} and 20 g L^{-1}, respectively.

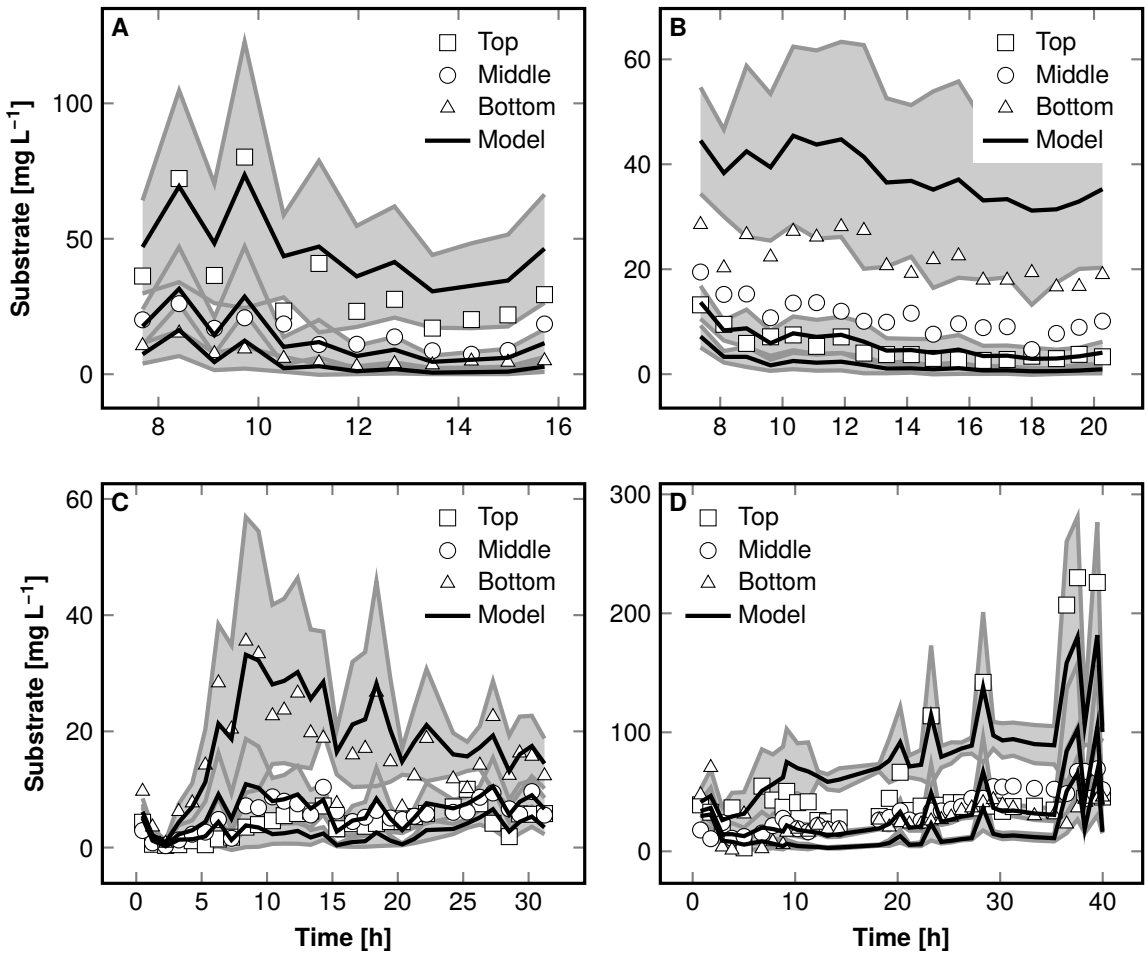

Figure 3: Model predictions and measured glucose concentrations in large-scale fermentations. The gray regions denote the estimated error of model prediction. (A) A 20 m^3 *S. cerevisiae* fermentation reported by Larsson et al. (1996). The glucose was fed at the top. (B) Otherwise the same setup as in panel A but with the glucose feed close to the bottom sampling port. (Larsson et al., 1996) (C) An 8 m^3 *E. coli* fermentation reported by Bylund et al. (1998). The glucose was fed close to the bottom port. (D) A 20 m^3 *E. coli* fermentation reported by Xu, Jahic, Blomsten, and Enfors (1999). The glucose was fed at the top.

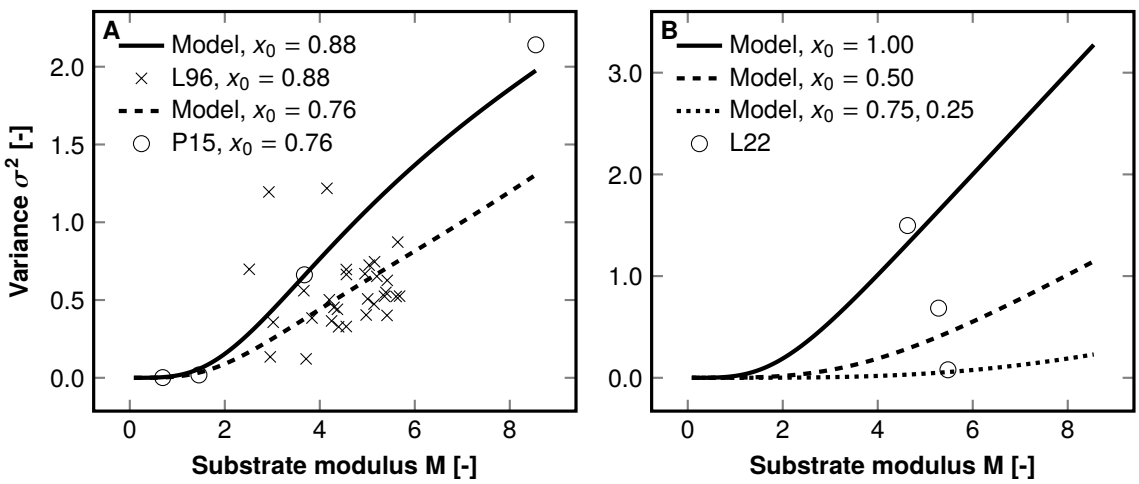

Figure 4: Volumetric variance of dimensionless substrate. (A) Experimental data by Larsson et al. (1996) (both top and bottom feeds, same set as in Figures 3A and 3B). Simulation data by Pigou and Morchain (2015). (B) Simulation data by Losoi et al. (2022).

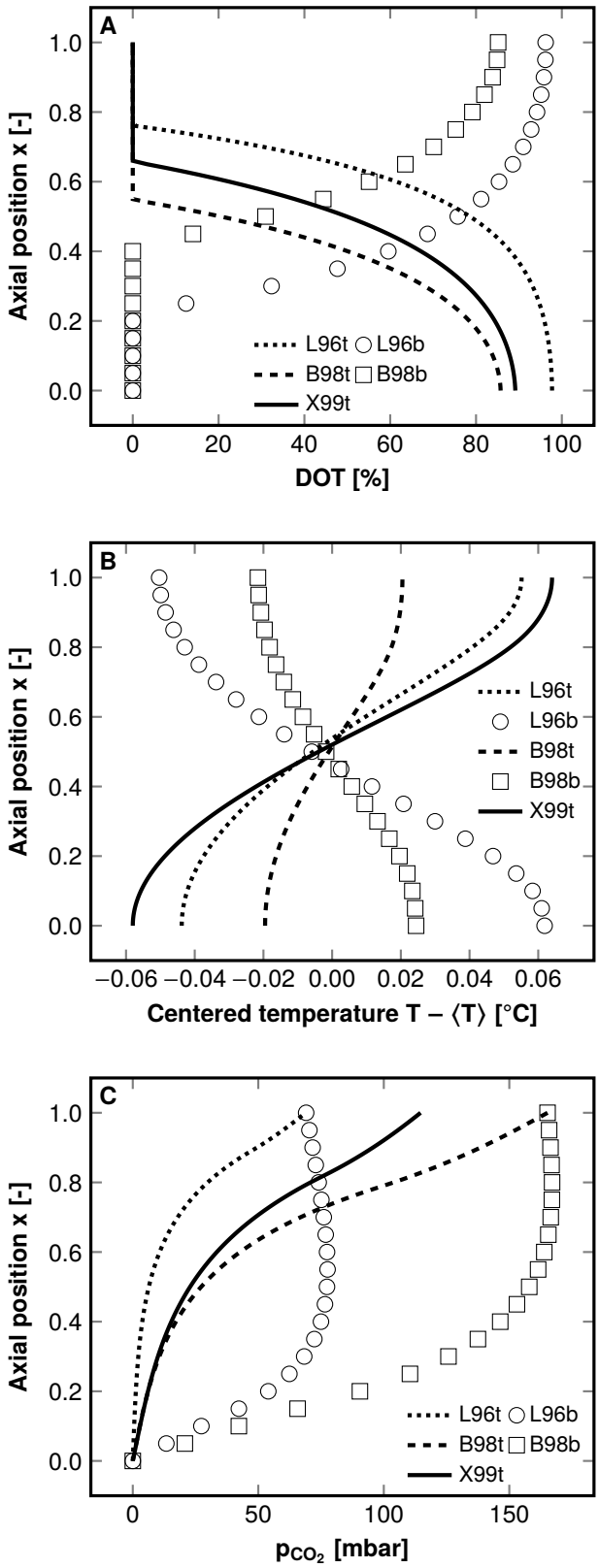

Figure 5: (A) Estimated dissolved oxygen distributions in large-scale cultivation experiments reported by Bylund et al. (1998), Larsson et al. (1996), and Xu, Jahic, Blomsten, and Enfors (1999). (B) Estimated temperature distributions in large-scale cultivation experiments reported by Bylund et al. (1998), Larsson et al. (1996), and Xu, Jahic, Blomsten, and Enfors (1999). (C) Estimated p_{CO_2} distributions in large-scale cultivation experiments reported by Bylund et al. (1998), Larsson et al. (1996), and Xu, Jahic, Blomsten, and Enfors (1999).

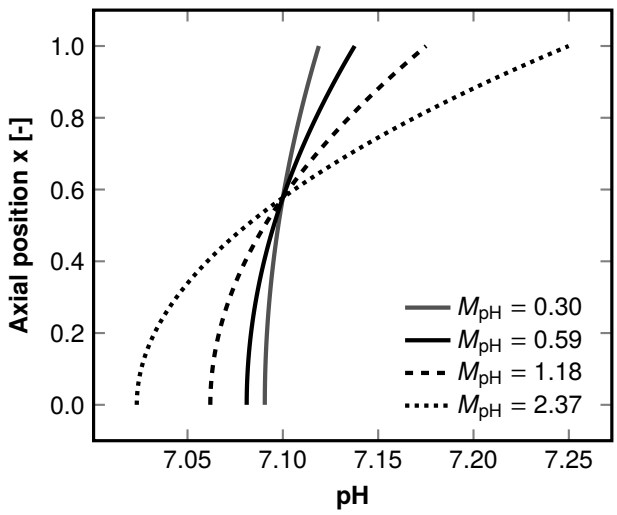

Figure 6: Axial profile of pH in a pseudo-steady state corresponding to the end of a control cycle that has raised pH from 6.9 to 7.1. The pH modulus M_{pH} = 0.59 corresponds to such a volume flow rate of the 25 % NH_4OH solution that equals the constant volume flow rate of the substrate feed in the Xu, Jahic, Blomsten, and Enfors (1999) large-scale experiment.